MNRAS 000, 1–14 (0000) Preprint 24 August 2016 Compiled using MNRAS LATEX style file v3.0

Inferring the IGM thermal history during reionisation with the Lyman-α forest power spectrum at redshift $z \simeq 5$

Fahad Nasir,[1]⋆ James S. Bolton,[1]† & George D. Becker [2]‡
[1]School of Physics and Astronomy, University of Nottingham, University Park, Nottingham, NG7 2RD, UK
[2]Department of Physics & Astronomy, University of California, Riverside, 900 University Avenue, Riverside, CA 92521, USA

arXiv:1605.04155v2 [astro-ph.CO] 23 Aug 2016

24 August 2016

ABSTRACT

We use cosmological hydrodynamical simulations to assess the feasibility of constraining the thermal history of the intergalactic medium during reionisation with the Lyα forest at $z \simeq 5$. The integrated thermal history has a measureable impact on the transmitted flux power spectrum that can be isolated from Doppler broadening at this redshift. We parameterise this using the cumulative energy per proton, u_0, deposited into a gas parcel at the mean background density, a quantity that is tightly linked with the gas density power spectrum in the simulations. We construct mock observations of the line of sight Lyα forest power spectrum and use a Markov Chain Monte Carlo approach to recover u_0 at redshifts $5 \lesssim z \lesssim 12$. A statistical uncertainty of ~ 20 per cent is expected (at 68 per cent confidence) at $z \simeq 5$ using high resolution spectra with a total redshift path length of $\Delta z = 4$ and a typical signal-to-noise ratio of $S/N = 15$ per pixel. Estimates for the expected systematic uncertainties are comparable, such that existing data should enable a measurement of u_0 to within ~ 30 per cent. This translates to distinguishing between reionisation scenarios with similar instantaneous temperatures at $z \simeq 5$, but with an energy deposited per proton that differs by 2–3 eV over the redshift interval $5 \lesssim z \lesssim 12$. For an initial temperature of $T \sim 10^4$ K following reionisation, this corresponds to the difference between early ($z_{\rm re} = 12$) and late ($z_{\rm re} = 7$) reionisation in our models.

Key words: dark ages, reionization, first stars – methods: numerical – intergalactic medium – quasars: absorption lines

1 INTRODUCTION

The intergalactic medium (IGM) probed by the Lyα forest of absorption lines is a valuable cosmic laboratory for studying the thermal and ionisation history of the Universe at redshifts $z \leq 7$. Observations of intergalactic absorption lines in high redshift quasar spectra indicate the first luminous sources had reionised the neutral hydrogen by $5.5 \leq z \leq 7$ and photo-heated the IGM to $\sim 10^4$ K (Becker et al. 2015a). The recently updated Thomson scattering optical depth reported by the Planck Collaboration et al. (2016) is furthermore consistent with an instantaneous reionisation at $z_{\rm re} = 8.8 \pm 0.9$. In combination with other, complementary observations, these observations translate to an HI reionisation era that may have started as early as redshift $z \sim 12$ and ended by $z = 5.5$–6 (Robertson et al. 2015; Bouwens et al. 2015; Mitra et al. 2015).

Despite this progress, details regarding the precise timing and duration of reionisation remain elusive. One possible approach to clarifying this situation is measuring the energy deposited into the low density IGM by photo-heating during reionisation (Miralda-Escudé & Rees 1994). At a redshift interval $\Delta z \simeq 1$–2 after reionisation the temperature of the low density ($\Delta = \rho/\bar{\rho} \leq 10$) IGM traced by the Ly$\alpha$ forest is expected to follow a power law relationship, $T = T_0 \Delta^{\gamma-1}$, parameterised in terms of the temperature at the mean cosmic gas density, T_0, and a slope, $\gamma - 1$ (Hui & Gnedin 1997; McQuinn & Upton Sanderbeck 2016). This temperature-density relation has been measured using a wide variety of techniques over the last two decades. These include analysing the velocity (Doppler) widths of Lyα absorption lines (Haehnelt & Steinmetz 1998; Schaye et al. 2000; Ricotti et al. 2000; McDonald et al. 2001; Rudie et al. 2012; Bolton et al. 2012, 2014), the suppression of small-scale power in the Lyα forest flux power spectrum (Zaldarriaga et al. 2001; Croft et al. 2002; Zaroubi et al. 2006; Viel et al. 2013a), the probability distribution of

⋆ E-mail: ppxfn@nottingham.ac.uk
† E-mail:james.bolton@nottingham.ac.uk
‡ E-mail: george.becker@ucr.edu

© 0000 The Authors

wavelet amplitudes (Meiksin 2000; Theuns & Zaroubi 2000; Zaldarriaga 2002; Lidz et al. 2010; Garzilli et al. 2012), the probability distribution of the transmitted Lyα forest flux (Lidz et al. 2006; Bolton et al. 2008; Calura et al. 2012; Lee et al. 2015), and the curvature of the Lyα forest transmission (Becker et al. 2011; Boera et al. 2014, 2016). The common element to almost all these studies is that they rely on mock Lyα forest spectra – typically drawn from cosmological hydrodynamical simulations – that can be compared directly to the observational data.

The bulk of these measurements are at redshifts $z < 4$ where high quality spectroscopic data are most readily available. These provide a valuable probe of photo-heating during the epoch of (likely quasar driven) HeII reionisation around $z \simeq 3$ (McQuinn et al. 2009; Compostella et al. 2014; Puchwein et al. 2015). Importantly, however, the long cooling timescale of the low density IGM enables T_0 measurements at $z \simeq 5-6$ to be used as a probe of HI reionisation at $z > 6$ (Haehnelt & Steinmetz 1998; Theuns et al. 2002; Hui & Haiman 2003; Trac et al. 2008; Cen et al. 2009; Furlanetto & Oh 2009; Lidz & Malloy 2014; D' Aloisio et al. 2015). Indeed, recent studies have demonstrated observational measurements of T_0 at $z = 5$–6 are inconsistent with rapid ($\Delta z \simeq 2$) late HI reionisation occurring at $z \lesssim 8$ (Raskutti et al. 2012; Upton Sanderbeck et al. 2015), although note this inference also depends on the typical spectral shape of the ionising sources during reionisation.

A wide range of reionisation scenarios therefore remain consistent with these data, and their constraining power remains relatively limited. Furthermore, the absorption features in the Lyα forest are not only sensitive to the instantaneous thermal state of the gas set by the Doppler broadening of the lines in velocity space. The absorbing gas is also smoothed out in physical space by the increased gas pressure following reionisation, leading to additional broadening of the absorption features (i.e. Jeans smoothing, Gnedin & Hui 1998; Hui & Rutledge 1999; Theuns et al. 2000; Peeples et al. 2010; Kulkarni et al. 2015; Garzilli et al. 2015). The long dynamical timescale for low density intergalactic gas (comparable to a Hubble time, e.g. Schaye 2001) means the precise degree of this pressure induced smoothing depends on the prior thermal (and hence reionisation) history. Consequently, the degeneracy between the Doppler broadening associated with the instantaneous gas temperature and the uncertain degree of pressure smoothing in the low density IGM is an important systematic for measurements of T_0 using the Lyα forest. It is furthermore a nuisance parameter when attempting to measure cosmological parameters and probe the nature of dark matter with the Lyα forest power spectrum (McDonald et al. 2006; Zaroubi et al. 2006; Viel et al. 2013a; Palanque-Delabrouille et al. 2015).

Analysis of the typical coherence scale of Lyα absorption transverse to the line of sight utilising close quasar pairs provides a promising way to directly measuring the pressure smoothing scale at $z \simeq 2$–3 (Rorai et al. 2013). However, the limited number of close pairs currently known at higher redshift prevents this method from being used at $z \simeq 5$, approaching the epoch of HI reionisation. The line of sight power spectrum of the transmitted flux at $z \simeq 5$ – a quantity widely studied at lower redshifts – provides a potential alternative. In common with other temperature diagnostics, the power spectrum is sensitive to *both* the instantaneous temperature and the prior thermal history. These smoothing scales may be disentangled to some extent with high resolution ($R \sim 40000$) spectra that probe wavenumbers $\log(k/\mathrm{km}^{-1}\,\mathrm{s}) \gtrsim -1$ (see e.g. Appendix D in Puchwein et al. 2015). As the quantity of high resolution Lyα forest data available at $z \simeq 5$ has increased in the last few years (e.g. Becker et al. 2015b, with 7 additional quasar spectra at $z > 5.8$ and 16 at $4.5 < z < 5.4$), a measurement of the cumulative energy deposited into the IGM, and hence tighter constraints on the thermal history during hydrogen reionisation may now be feasible (see also Lidz & Malloy 2014).

In this work, we demonstrate that it is possible to constrain the integrated thermal history at $z > 5$ using the Lyα forest power spectrum measured from data sets that are now comparable in size to existing high resolution observational measurements. Recent studies have typically parameterised the integrated thermal history in Lyα forest models as either a characteristic filtering scale, k_F, over which the gas is smoothed (e.g Rorai et al. 2013), or as the starting redshift of reionisation, z_re, in optically thin hydrodynamical simulations (Viel et al. 2013a). The former approach is well motivated, but in practice often treats the pressure smoothing scale as a free parameter that is decoupled from the reionisation history. The latter approach is not optimal either, as the parameter z_re does not uniquely define[1] the amount of energy deposited into the IGM as a function of time. In this work we propose instead that, aided by a suitable grid of hydrodynamical models, one may instead infer the cumulative energy per proton injected into a gas parcel during and soon after reionisation – a quantity which is more straightforward to connect directly to reionisation models.

The structure of this paper is as follows. In Section 2, we present an overview of the hydrodynamical simulations used in this work and examine the typical scales on which thermal broadening and pressure smoothing act on the Lyα forest power spectrum at $z \simeq 5$. In Section 3, we examine the relationship between the gas density and Lyα forest transmission power spectra and the cumulative energy per proton injected into the IGM at mean density, u_0. In Section 4, we forecast how well observations might distinguish between different integrated thermal histories by examining mock datasets within a Bayesian statistical framework via a Markov Chain Monte Carlo (MCMC) analysis. We finally summarise our conclusions in Section 5. Throughout this paper we refer to comoving Mpc and kpc as "cMpc" and "ckpc", respectively. A flat ΛCDM cosmology is adopted thoughout, with $\Omega_\mathrm{m} = 0.26$, $\Omega_\Lambda = 0.74$, $\Omega_\mathrm{b}h^2 = 0.023$, $\sigma_8 = 0.80$, $h = 0.72$ and $n_\mathrm{s} = 0.96$.

2 MODELLING THE Lyα FOREST AT $z \simeq 5$

2.1 Hydrodynamical simulations

In order to model Lyα forest spectra at $z \simeq 5$ we first require hydrodyanmical simulations with a variety of thermal histories. The models used in this work are summarised in Table 1, and are described in Becker et al. (2011) and

[1] For example, two reionisation models where z_re is identical but the spectral shape of the ionising sources is different will not have the same thermal history.

Table 1. The hydrodynamical simulations used in this work. All models have a box size of $10h^{-1}$ cMpc, 2×512^3 particles and a gas particle mass of $9.2\times10^4 h^{-1}M_\odot$. The columns in the table list the redshift of reionisation, z_{re}, in the model, the scaling factors for the photoheating rates (see text for details), the logarithm of the temperature at mean density $\log T_0$, the slope of the temperature-density relation, γ, and the cumulative energy per proton, u_0, deposited into a gas parcel at mean density by $z=4.9$. The values of $\log T_0$ and γ are estimated with a power-law fit to the volume weighted temperature-density plane.

Model	z_{re}	ζ	ξ	$\log(T_0^{z=4.9}/\mathrm{K})$	$\gamma^{z=4.9}$	$u_0^{z=4.9}$ [eV m$_p^{-1}$]	References
A15	9	0.30	0.00	3.68	1.43	3.1	Table 2, Becker et al. (2011)
B15	9	0.80	0.00	3.98	1.46	5.9	
C15	9	1.45	0.00	4.16	1.47	8.7	
D15	9	2.20	0.00	4.28	1.48	11.5	
E15	9	3.10	0.00	4.38	1.47	14.5	
F15	9	4.20	0.00	4.47	1.47	17.8	
G15	9	5.30	0.00	4.53	1.48	20.9	
D13	9	2.20	-0.45	4.28	1.37	11.5	
D10	9	2.20	-1.00	4.26	1.08	11.5	
D07	9	2.20	-1.60	4.25	0.92	11.5	
Tz15	15	–	–	3.92	1.49	12.4	Appendix B, Becker & Bolton (2013)
Tz12	12	–	–	3.93	1.50	9.3	
Tz9	9	–	–	3.92	1.50	5.2	
Tz7	7	–	–	3.93	1.47	3.7	
Tz9HOT	9	–	–	4.21	1.52	11.3	

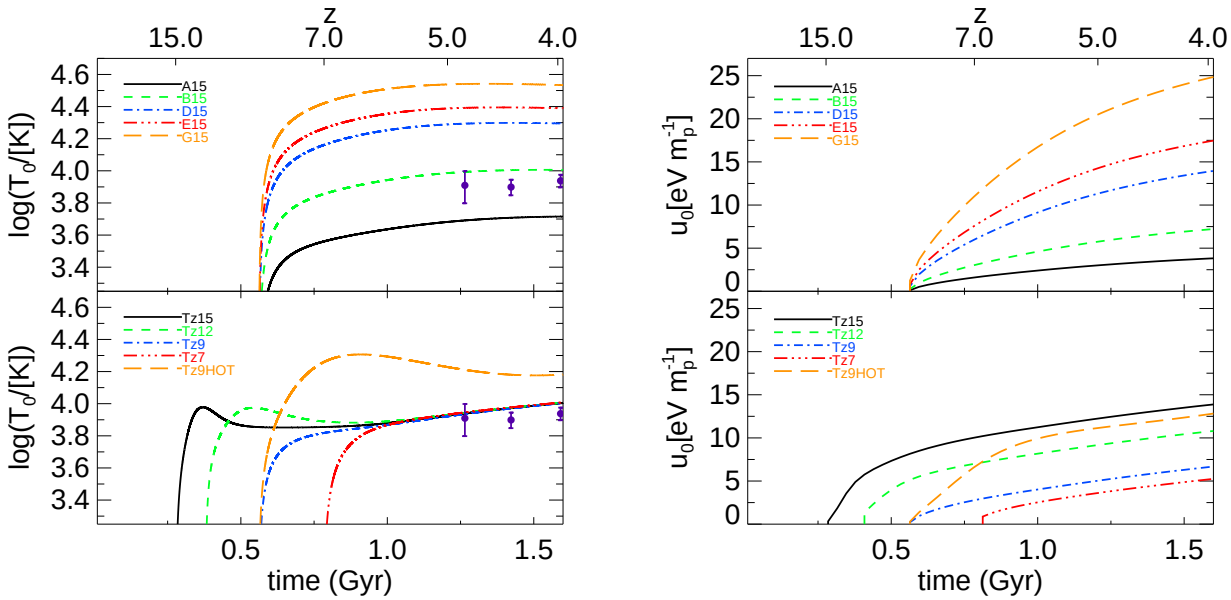

Figure 1. *Left:* The logarithm of the temperature at mean density, T_0, as function of time for a subset of the simulations listed in Table 1. The T_0 observational measurements from Becker et al. (2011), evaluated at their fiducial γ values along with 2σ errors, are shown by the filled circles. *Right:* The cumulative energy per proton deposited in a gas parcel at mean density (see Section 3 for details) as a function of time in the simulations.

Becker & Bolton (2013). Convergence tests with box size and mass resolution are presented in those papers and in Bolton & Becker (2009).

In brief, the simulations were performed with the smoothed-particle hydrodynamics code P-Gadget-3, an updated version of the publicly available Gadget-2 (Springel 2005). These simulations use a total of 2×512^3 dark matter and gas particles within a periodic $10h^{-1}$ cMpc box. The initial positions and velocities of the particles at redshift $z=99$ were generated using the P-Genic initial conditions code (Springel et al. 2005) and the Eisenstein & Hu (1999) transfer function. In this work we neglect the impact of the small change in cosmological parameters required to match the more recent results reported by the Planck Collaboration et al. (2015), but expect that this will not affect our general conclusions. The baryons in the Lyα forest simulations are of primordial composition with a helium fraction by mass of $Y=0.24$ (Olive & Skillman 2004). Any gas particles with an overdensity $\Delta>10^3$ and temperature $T<10^5$ K are converted to collisionless star par-

ticles (Viel et al. 2004). The gas is also photo-ionised and heated by a spatially uniform metagalactic UV background (UVB) applied in the optically thin limit. The gas is assumed to be in ionisation equilibrium (Katz et al. 1996) using the recombination, ionisation and cooling rates listed in Bolton & Haehnelt (2007).

The UVB for the Becker et al. (2011) simulations is based on the Haardt & Madau (2001) synthesis model. This includes ionising emission from young star forming galaxies and quasars, and results in rapid reionisation at $z_{\rm re} = 9$. The photo-heating rates in most of these models have been rescaled to reproduce a range of temperature-density relations, such that $\epsilon_{\rm i} = \zeta \Delta^{\xi} \epsilon_{\rm i}^{\rm HM01}$, where $\epsilon_{\rm i}^{\rm HM01}$ are the Haardt & Madau (2001) photoheating rates for species $i = [{\rm H\,I}, {\rm He\,I}, {\rm He\,II}]$ and ζ, ξ are constants listed in Table 1. We also include five simulations from Becker & Bolton (2013). These have UVB models that have been tuned by hand to reproduce a range of reionisation histories. Four of the models are designed to have similar temperatures at $z \simeq 5$ that match the Becker et al. (2011) IGM temperature measurements, but with $z_{\rm re} = [15, 12, 9, 7]$. The final model, Tz9HOT, is similar to Tz9 but with increased photo-heating rates. The evolution of the temperature and the cumulative energy per proton deposited in a gas parcel at the mean background density (see Eq. (4) and Section 3 for details) in these models is displayed in Fig. 1.

In order to extract mock spectra from our simulations we analyse snapshots at $z = 4.915$. The spectra consist of 2048 pixels drawn along 1000 random sight-lines parallel to the box boundaries. The mean transmission, $\langle F \rangle$, of the spectra is rescaled to correspond to an effective optical depth $\tau_{\rm eff} = -\ln\langle F \rangle = 1.53$ (Fan et al. 2006; Becker et al. 2013), and the spectra are convolved with a Gaussian instrumental profile with FWHM $= 7\,{\rm km\,s^{-1}}$. In order to aid intuition, Fig. 2 demonstrates the range of gas densities the Lyα forest is sensitive to at $z = 4.9$. We plot the optical depth weighted gas overdensity, Δ_τ (Schaye et al. 1999), against the transmitted flux from the D15 model. The Lyα forest at high redshift predominately probes gas close to the mean background density, with very little contribution from regions with overdensities greater than a few except where the transmission is saturated ($F = 0$). This may be contrasted to the Lyα forest at $z = 2$–3, where the bulk of the transmission arises from mildly overdense gas (cf. fig. 4 in Bolton et al. 2014).

Finally, before proceeding further we note that one caveat to our analysis is that reionisation is an inhomogeneous process and spatial fluctuations in the IGM temperature and pressure smoothing scale are expected during reionisation (Raskutti et al. 2012; Lidz & Malloy 2014; D' Aloisio et al. 2015). Our $10h^{-1}$ cMpc simulation boxes are too small to capture this effect – this scale is comparable to the typical size of individual H II regions during reionisation (e.g. Wyithe & Loeb 2004; Furlanetto et al. 2006) – but for this reason approximating a uniform redshift of reionisation over this volume is likely reasonable. The large scales on which temperature fluctuations occur also translate to a modest effect (< 5 per cent) on the one dimensional power spectrum (Lai et al. 2006; McQuinn et al. 2011; Greig et al. 2015). A direct comparison of the gas clumping factor predicted by radiation hydrodynamical simulations performed in similar volumes to this work (Finlator et al. 2012) to optically thin models (Pawlik et al. 2009) also yields good agreement (see fig. 5 in Finlator et al. 2012). Nevertheless, full radiation hydrodynamical simulations that model patchy reionisation may eventually be required. The first steps toward such large scale simulations are being made (Gnedin 2014; Norman et al. 2015; Pawlik et al. 2015; Park et al. 2016), although attaining the required mass resolution for modelling the high redshift Lyα forest in large volumes remains challenging.

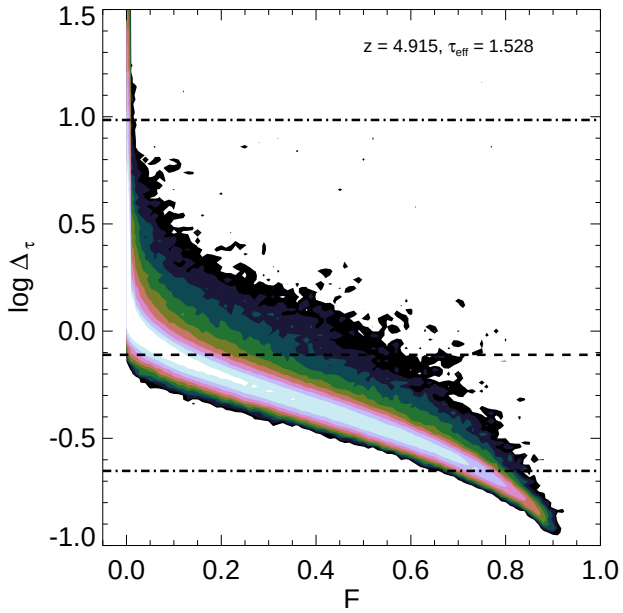

Figure 2. Contour plot of the optical depth weighted gas overdensity, Δ_τ, against transmitted flux F at $z = 4.9$ for the D15 model for $\tau_{\rm eff} = 1.53$. Here Δ_τ is calculated as a weighted average $\Delta_{\rm i} = \sum \tau_{\rm i} \Delta_{\rm i} / \sum \tau_{\rm i}$, where $\Delta_{\rm i}$ and $\tau_{\rm i}$ are the gas overdensity and optical depth at the ith pixel on each sightline (Schaye et al. 1999). The number density of pixels increase by 0.5 dex within each contour level. The dashed and dot-dashed lines display the median and 95 per cent range of the optical depth weighted densities.

2.2 The broadening of Lyα forest absorbers

In this section we briefly review the impact of thermal broadening and pressure smoothing on the Lyα forest power spectrum at $z \simeq 5$ (see also Bi et al. 1992; Peeples et al. 2010; Kulkarni et al. 2015; Garzilli et al. 2015; Puchwein et al. 2015). We begin with the assumption that Lyα absorbers are in hydrostatic equilibrium (Schaye 2001). The scale where the dynamical time equals the sound crossing timescale is the Jeans scale, $L_{\rm J}$, which may also be written in terms of a line of sight velocity, $\sigma_{\rm J} = H(z) L_{\rm J}$, where $L_{\rm J}$ is a proper distance. For gas with temperature T and normalised density Δ, this corresponds to:

$$\begin{aligned} \sigma_{\rm J} &= \left(\frac{40\pi^2 k_{\rm B}}{9 \mu m_{\rm H}} \right)^{1/2} T^{1/2} \Delta^{-1/2} \left(\frac{\Omega_{\rm m}(1+z)^3 + \Omega_\Lambda}{\Omega_{\rm m}(1+z)^3} \right)^{1/2} \\ &\approx 77.1 {\rm km\,s^{-1}} \left(\frac{\rm T_0}{10^4 {\rm K}} \right)^{1/2} \Delta^{\gamma/2-1}, \end{aligned} \tag{1}$$

where we assume $\mu = 0.61$ for the mean molecular weight of an admixture of ionised hydrogen and singly ionised he-

lium[2]. In the second line we have also used the fact that $T = T_0\Delta^{\gamma-1}$ and $\Omega_{\rm m}(1+z)^3 \gg \Omega_\Lambda$ at $z \gtrsim 3$. Note, however, the Jeans scale only approximates the pressure smoothing scale in the low density IGM. As the dynamical timescale, $t_{\rm dyn} = \sqrt{\pi/G\rho_{\rm m}} \simeq H(z)^{-1}\Delta^{-1/2}$, is long for low density gas the absorbing structures in the Lyα forest at $z \simeq 5$ will not have reached hydrostatic equilibrium. The pressure smoothing scale is instead better described as $\sigma_{\rm p} = f_{\rm J}\sigma_{\rm J}$, where $f_{\rm J} < 1$ and depends on the prior thermal history (Gnedin & Hui 1998; Hui & Rutledge 1999, and see footnote 2).

In comparison, the thermal (or Doppler) broadening scale for a Gaussian line profile is given by:

$$\sigma_{\rm th} = \left(\frac{k_{\rm B}T}{m_{\rm H}}\right)^{1/2} = 9.1{\rm km\,s^{-1}}\left(\frac{\rm T_0}{10^4\,{\rm K}}\right)^{1/2}\Delta^{(\gamma-1)/2}. \quad (2)$$

The ratio of these two scales is $\sigma_{\rm p}/\sigma_{\rm th} \simeq 8.5 f_{\rm J}\Delta^{-1/2}$. In general we therefore expect the pressure smoothing to act on similar scales to the thermal broadening. Fortunately, as we see shall see next, the different scale dependence of these effects in our hydrodynamical simulations at $z = 5$ enables us to break this degeneracy.

2.3 The line of sight Lyα forest power spectrum

We compute the power spectrum of the transmitted flux, $P_{\rm F}(k)$, at $z = 4.9$ from our simulations using the estimator $\delta_{\rm F} = F/ < F > -1$, where $\langle F\rangle = \langle e^{-\tau}\rangle$ is the mean transmission (or equivalently the effective optical depth, $\tau_{\rm eff} = -\ln\langle F\rangle = 1.53$) of the 1000 sight-lines drawn from each simulation. The top row of Fig. 3 shows the results for a subset of the models listed in Table 1. The left hand panel displays the effect of changing T_0 on the power spectrum; higher temperatures result in decreased power at wavenumbers $\log(k/{\rm km^{-1}\,s}) > -1.5$ arising from a combination of thermal broadening and pressure smoothing. The middle panel demonstrates the effect of changing γ – the slope of the temperature-density relation – is more modest, with a slight increase in power over all scales as γ is decreased. This is in part due to the fact that the typical gas densities probed by the Lyα forest at $z \simeq 5$ are close to mean density, and the characteristic pressure and thermal broadening scales both have a modest dependence on gas density. It also suggests that any constraint on γ from $P_{\rm F}(k)$ is likely to be weak at this redshift.

The right panel in the top row displays the four models with varying $z_{\rm re}$; recall these have similar T_0 at $z = 4.9$ but different reionisation redshifts. Any differences in $P_{\rm F}(k)$ are due variations in the pressure smoothing scale only. The Tz15 model has less power (and more pressure smoothing) than the Tz7 and Tz9 models over a wide range of wavenumbers, with the largest differences at $\log(k/{\rm km^{-1}\,s}) \simeq -1$. Earlier reionisation allows more time for the gas to respond to the change in pressure due to heating during and soon after reionisation, resulting in increased smoothing of the gas distribution. Note also the power spectra for the Tz15 and Tz12 models are very similar, although the cumulative energy per proton deposited at mean density, u_0, by $z = 4.9$ in these models is rather different. A related result was noted by Pawlik et al. (2009), who found that the clumping factor[3], $C = \langle\rho^2\rangle/\bar{\rho}^2$, of gas in optically thin hydrodynamical simulations at $z \approx 6$ is insensitive to the redshift of reionisation if $z_{\rm re} \geq 9$. Although the exact upper redshift limit will be model dependent, this indicates the pressure smoothing is only sensitive to the prior IGM thermal history over a limited redshift range (see also Figure 8 and text in Section 5).

We may examine the impact of pressure smoothing and thermal broadening on the Lyα forest power spectrum more easily by separating these effects in our models. We first fit a single power law to the $T-\Delta$ relation in each model, with $\log T_0$ and $\gamma-1$ as the intercept and slope. We then translate and rotate the entire $T-\Delta$ plane in each simulation to match $\log T_0$ and $\gamma-1$ from another model. This procedure allows us to change the instantaneous temperature of the gas, but retain the same pressure smoothing scale (which arises from the underlying gas density distribution). The middle row in Fig. 3 displays the result of this procedure, where we have transformed each $T-\Delta$ plane in each model to correspond to the T_0 and γ values in the D15 simulation in the left and middle column, and the Tz15 model in the right. Note that as the temperatures are changed we also rescale the neutral hydrogen number densities in the simulated spectra as $n_{\rm HI} \propto T^{-0.72}$, due to the temperature dependence of the H II recombination coefficient (Verner & Ferland 1996). All models are again rescaled to have the same $\tau_{\rm eff} = 1.53$.

As might be expected, the different thermal histories in the simulations displayed in the middle left panel of Fig. 3 produce rather different pressure smoothing scales. With the effect of thermal broadening removed, this effect is most prominent at wavenumbers $0.03 \leq k/[{\rm km^{-1}\,s}] \leq 0.13$, shown by the dashed vertical lines, although it operates to a lesser extent at smaller scales (i.e. larger wavenumbers) as well. In contrast, the central panel demonstrates the slope of the $T-\Delta$ relation has very little impact on the pressure smoothing except at the smallest scales – note the cumulative energy per proton deposited into a gas parcel at mean density is identical in these simulations. The models with varying $z_{\rm re}$ are also largely unchanged, emphasizing again that it is the pressure smoothing which causes the differences in the power spectrum for these models.

Finally, the bottom row of Fig. 3 displays the flux power spectrum computed using the density field from the D15 model (left and middle panel) and the Tz15 model (right panel), but with an imposed $T-\Delta$ relation that matches the models indicated in the figure panels. This procedure isolates the impact of thermal broadening on $P_{\rm F}(k)$. There is some degeneracy with the pressure smoothing, but in general the

[2] The Jeans scale in Eq. (1) is larger than the classical cosmological Jeans scale, $\lambda_{\rm J}$ – derived from linear theory when assuming an adiabatic thermal history – by a factor of 2π (Bi et al. 1992; Kulkarni et al. 2015). For arbitrary thermal histories within the linear theory derivation, Gnedin & Hui (1998) further show that the pressure smoothing may be described by a filtering scale, $\lambda_{\rm F}$, which depends on the prior thermal history. Typically $\lambda_{\rm F} < \lambda_{\rm J}$ and $\lambda_{\rm F} \sim 100\,{\rm ckpc}$ ($\sim 10\,{\rm km\,s^{-1}}$ at $z = 5$), although the precise value is dependent on the prior heating history of the IGM.

[3] The clumping factor is related to the root mean square of the density contrast (and hence also the gas density power spectrum) by $\langle\delta^2\rangle = C-1$, where the density contrast is $\delta = \rho/\bar{\rho}-1$.

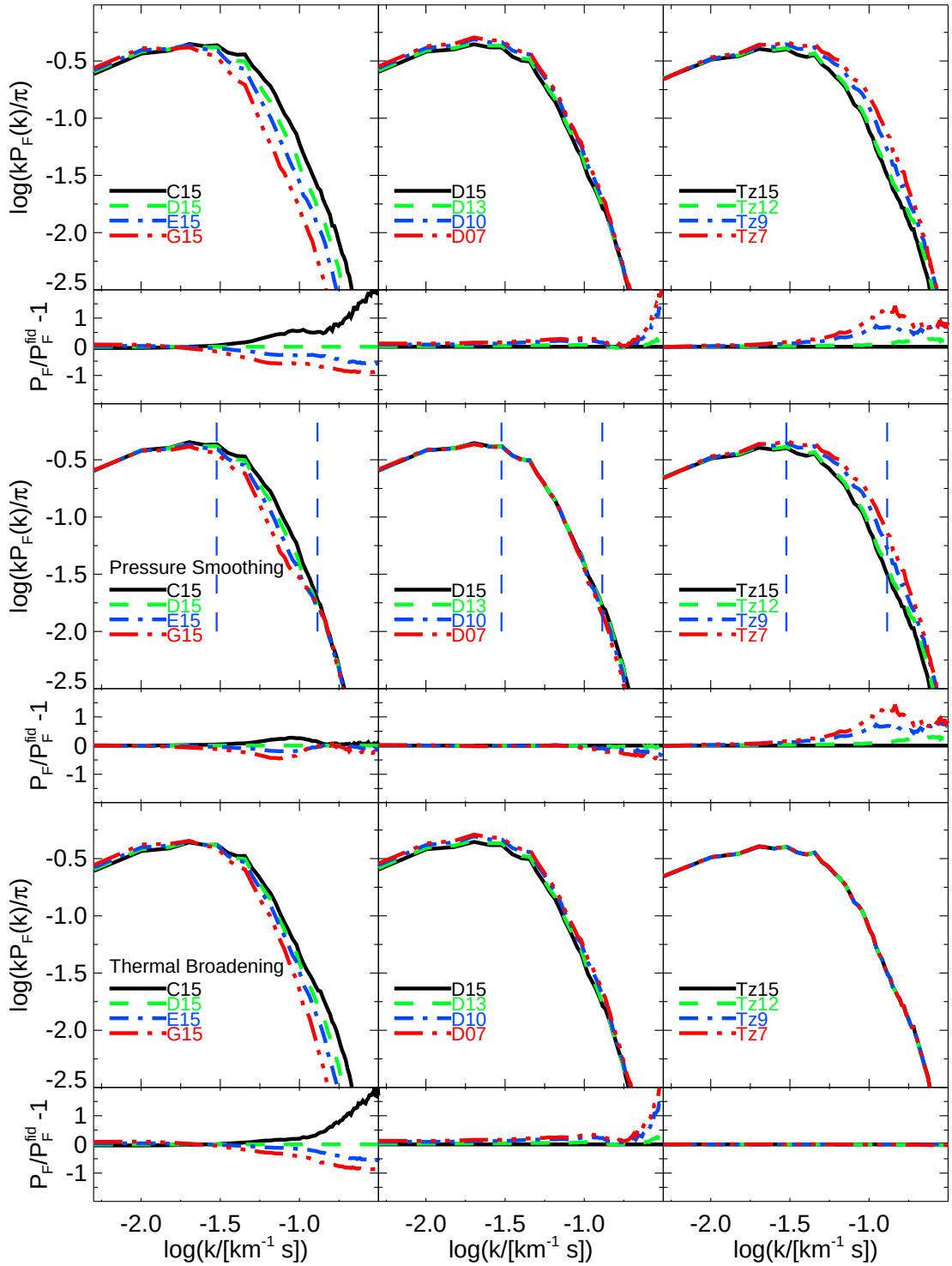

Figure 3. *Top row:* the transmitted flux power spectrum – including variations from both pressure smoothing and thermal broadening – at $z = 4.9$ for a sub-set of models with varying T_0 (left), γ (middle) and the redshift of reionisation (right). The power spectra are displayed relative to the D15 (left and middle) and Tz15 (right) models are displayed immediately below. *Middle row:* the power spectrum for the same simulations, but now with each $T-\Delta$ relation mapped to the D15 (left and middle) and the Tz15 model (right). The thermal broadening in these models is therefore identical. The dashed blue lines display the approximate wavenumber range over which pressure smoothing is dominant. Note that for simulations with varying γ (D15-D07, middle column), pressure smoothing has very little effect on the power spectrum except at the smallest scales. *Bottom row:* the transmitted flux power spectrum for the D15 (left and middle) and Tz15 (right) models after imposing the $T-\Delta$ relation from the models indicated in the figure legend. The pressure smoothing in these models is identical. The varying $z_{\rm re}$ models have almost identical values of T_0 at $z \sim 4.9$ (Fig. 1) and therefore are indistinguishable when pressure smoothing is removed. This can be seen by comparing middle-right and bottom-right panels. The u_0, T_0 and γ values for each model are listed in Table 1. All mock spectra are scaled to have $\tau_{\rm eff} = 1.53$, and have been convolved with a Gaussian with FWHM=7km s^{-1}.

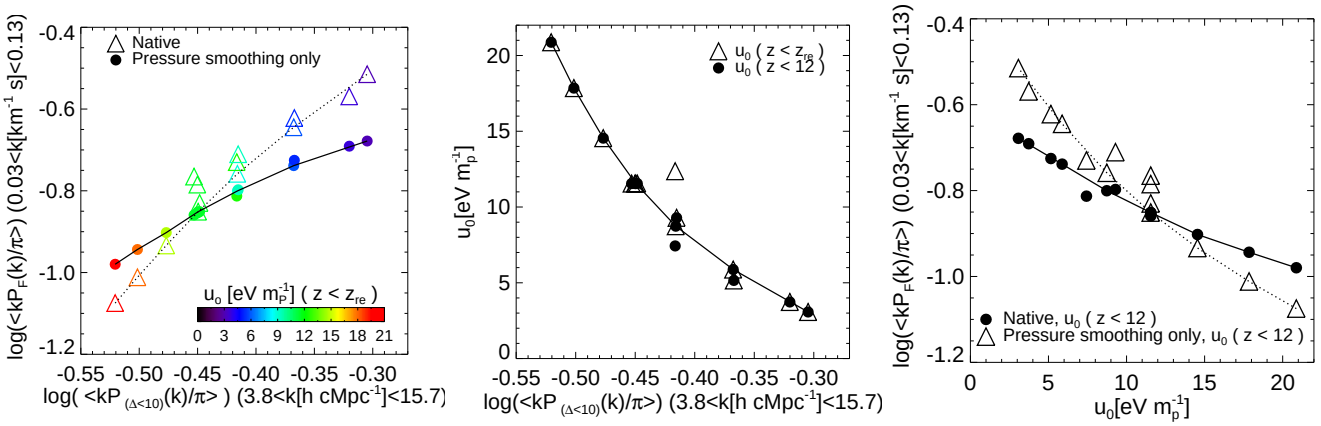
Native
Pressure smoothing only
u0 [eV mp-1] (z < zre)
0 3 6 9 12 15 18 21
log(<kP F(k)/π>) (0.03<k[km-1 s]<0.13)
log(<kP (Δ<10)(k)/π>) (3.8<k[h cMpc-1]<15.7)
u0 (z < zre)
u0 (z < 12)
u0[eV mp-1]
Native, u0 (z < 12)
Pressure smoothing only, u0 (z < 12)

Figure 4. *Left:* The open triangles display the average of the Lyα forest power spectrum at wavenumbers $0.03 < \mathrm{k/km^{-1}\,s} < 0.13$ (approximately the scale where pressure smoothing dominates) against the $\Delta < 10$ gas density power spectrum averaged over the equivalent scale. The A15–G15, Tz15–Tz7 and D13–D07 models are shown at $z = 4.9$, with a dotted curve through the A15–G15 models. The average Lyα forest power spectrum for each model after thermal broadening differences are removed is shown by the filled circles. Here each $T-\Delta$ distribution is mapped to the T_0 and γ for the D15 model, and a solid curve is drawn through the A15–G15 models. The colour scale indicates u_0 for each model. *Centre:* The cumulative energy per proton against the average of the $\Delta < 10$ density power spectrum computed using Eq. (4) for all photo-heating up to $z_{\rm re}$ for each model (open triangles) and $z = 12$ (filled circles). The solid curve is again drawn through the A15–G15 models. *Right:* The average of the Lyα forest flux power spectrum at wavenumbers $0.03 < \mathrm{k/km^{-1}\,s} < 0.13$ (open triangles) against $u_0(z < 12)$. The filled circles show the same quantity once differences due to thermal broadening are removed. The solid and dashed curves are again drawn through A15–G15 models.

thermal broadening acts on smaller scales, with the largest difference in the models occurring at $\log(k/\mathrm{km^{-1}\,s}) > -1$. The small-scale cut-off for the power spectrum is mainly determined by the instantaneous temperature (Peeples et al. 2010). This also suggests that measurements of the power spectrum at small scales, $-1 \leq \log(k/\mathrm{km^{-1}\,s}) \leq -0.5$, are required to break the degeneracy between pressure smoothing and thermal broadening. Note also the models in the middle panel are similar to the results in the top row; most of the contribution to the power when changing γ is from thermal broadening. As expected, there is no apparent difference in power among the varying $z_{\rm re}$ models, which are designed to reach a similar temperature at mean density around $z \simeq 5$.

3 FROM FLUX POWER SPECTRUM TO THERMAL HISTORY

We now proceed to examine the relationship between the transmitted flux power spectrum at $z \simeq 5$ and the integrated thermal history in our hydrodynamical simulations. The temperature evolution of a gas parcel with density ρ in an expanding universe can be expressed as (e.g. Miralda-Escudé & Rees 1994; McQuinn & Upton Sanderbeck 2016)

$$\frac{dT}{dt} = \frac{2\mu m_H}{3k_B\rho}(\mathscr{H} - \Lambda) + \frac{2T}{3(1+\delta)}\frac{d\delta}{dt} + \frac{T}{\mu}\frac{d\mu}{dt} - 2HT, \qquad (3)$$

where $\mathscr{H} = \sum_i n_i \varepsilon_i$ is the total photoheating rate per unit volume for the species $i = [\mathrm{H\,I}, \mathrm{He\,I}, \mathrm{He\,II}]$, Λ is the cooling rate per unit volume, and H is the Hubble parameter. The first term in Eq. (3) encapsulates all the photo-heating and radiative cooling processes. The second term describes adiabatic heating and cooling from structure formation, and the third term is associated with changes in the mean molecular weight. The final term arises from adiabatic cooling due to the expansion of the Universe.

The cumulative energy deposited into a gas parcel by photo-heating is obtained by considering the first term in Eq. (3) and setting the radiative cooling term to zero. Noting that the specific internal energy is given by $u = 3k_BT/2\mu m_{\rm H}$, we may then write $du/dt = \mathscr{H}/\rho$. For a gas parcel at the mean background density, the total energy per unit mass deposited into the gas parcel by redshift z_0 is

$$u_0 = \int_{z_0}^{z_{\rm re}} \frac{\mathscr{H}}{\bar{\rho}} \frac{dz}{H(z)(1+z)}, \qquad (4)$$

where $\bar{\rho} = \rho_{\rm crit}\Omega_{\rm b}(1+z)^3$ is the mean background baryon density. This quantity is displayed in the left panel of Fig. 1 and is listed in Table 1 at $z = 4.9$. The cumulative energy per proton deposited into a gas parcel at mean density is straightforward to compute for a given reionisation history in our Lyα forest simulations.

We illustrate the relationship between the transmitted flux power spectrum, the gas density power spectrum and u_0 in our hydrodynamical simulations in Fig. 4. The open triangles in the left panel display the mean of the transmitted flux power spectrum against the mean of the gas density power spectrum for all gas with $\Delta < 10$. The mean is obtained over the scales $0.03 \leq k/[\mathrm{km^{-1}\,s}] \leq 0.13$, approximately corresponding to the scales over which the influence of pressure smoothing is largest in our models (see Fig. 3). Following Kulkarni et al. (2015) and Lukić et al. (2015), we consider the gas density power spectrum for normalised densities $\Delta < 10$ only; including higher density gas associated with non-linear structure results in significantly more power toward small scales. As shown in Fig. 2, the Lyα forest power spectrum at $z \simeq 5$ is insensitive to absorption from gas at these densities. The precise choice of cut-off here is somewhat arbitrary, but is motivated by the fact that optical

depth weighted densities, $0.2 \leq \Delta_\tau \leq 10$, bound 95 per cent of all Lyα forest pixels at $z = 4.9$ in our models.

There is a correlation between the Lyα forest power spectrum and the underlying gas density power spectrum, as expected. Models with a greater energy deposited per proton exhibit less power on scales $0.03 \leq k/(\mathrm{km^{-1}\,s}) \leq 0.13$ due to the smoother distribution of gas. The points that scatter upward from the dotted curve correspond to the varying γ and $z_{\rm re}$ models. The increased power in the transmitted flux arises from differences in the thermal broadening, even for models where the average gas density power spectrum (and energy input per proton) are similar. The pressure smoothing is thus still somewhat degenerate with thermal broadening on these scales. This is evident from the filled circles in the left panel of Fig. 4, which display the average Lyα forest power spectrum after rescaling the T–Δ relation in all models to match the D15 simulation. This implies if the degeneracy between thermal broadening and pressure smoothing is broken with the transmitted flux power spectrum on scales $\log(k/\mathrm{km^{-1}\,s}) > -1$, the Ly$\alpha$ forest directly probes the underlying gas density power spectrum (or equivalently the gas clumping factor[4]) at $z \simeq 5$.

The open triangles in the centre panel of Fig. 4 display the cumulative energy deposited per proton at mean density, u_0, computed using Eq. (4) against the gas density power spectrum for $\Delta < 10$. The gas density power spectrum is averaged over the same scale as in the left panel. Again, there is an excellent correlation between the two quantities aside from the triangle at $u_0 = 12.4\,\mathrm{eV\,m_p^{-1}}$ corresponding to the Tz15 model with $z_{\rm re} = 15$. All the other models experience rapid reionisation at $z \leq 12$. As discussed earlier, this is because the thermal history at $z > 12$ does not significantly impact on the pressure smoothing scale of the gas in our simulations. This is illustrated by the filled circles in the right panel, which show u_0 computed at $z \leq 12$ only.

Finally, the open triangles in the right panel of Fig. 4 display the correlation between the average flux power spectrum on scales $0.03 \leq k/(\mathrm{km^{-1}\,s}) \leq 0.13$ and u_0 at $z < 12$. Note again there is some degeneracy with thermal broadening when averaging on these scales; the filled circles show the same quantity once differences due to thermal broadening are removed. This simple analysis suggests that $u_0(z \lesssim 12)$ should serve as a convenient and useful parameterisation for the prior thermal history in our simulations. A more rigorous approach requires analysing the full Lyα forest power spectrum and correctly dealing with the parameter degeneracies in the model, which we turn to next.

4 INFERRING THE THERMAL HISTORY DURING REIONISATION

4.1 Markov Chain Monte Carlo analysis

We make forecasts for the constraints attainable on the thermal history using a Bayesian MCMC approach. Given a set of power spectrum measurements, $P_{\rm F}^{\rm data}$, we maximise the likelihood function, $\mathcal{L}$, with respect to the model parameters used in our hydrodynamical simulations, M, (e.g. Zaroubi et al. 2006; Viel et al. 2009; Rorai et al. 2013)

$$\ln \mathcal{L}(P_{\rm F}^{\rm data}|M) \propto (P_{\rm F}^{\rm data} - P_{\rm F}^{\rm model})^T \Sigma_{\rm data}^{-1} (P_{\rm F}^{\rm data} - P_{\rm F}^{\rm model}). \quad (5)$$

Here $P_{\rm F}^{\rm model}$ is the simulated Lyα forest power spectrum for a given set of model parameters M, while $\Sigma_{\rm data}$ is the covariance matrix for the measured power spectrum.

We consider four parameters in our analysis – $\log T_0$, u_0, γ and $\tau_{\rm eff}$ – and vary these to construct grid of models based on our A15–G15 simulations. We obtain combinations of the three thermal parameters by imposing different T–Δ relations on the simulations, as described in Section 2.3. In this way we retain the gas density power spectrum associated with a given value of u_0 in our models while varying the instantaneous temperature. We consider seven values for for the cumulative energy deposited per proton over the range $u_0 = 3.1$–$20.9\,\mathrm{eV\,m_p^{-1}}$, following the parameter range covered by our hydrodynamical simulations[5]. The T–Δ relation is varied over $\log(T_0/\mathrm{K}) = 3.6$–$5.0$ and $\gamma = 0.6$–1.8. The former range is consistent with estimates of the IGM temperature at mean density at $z \simeq 5$, while the latter encompasses physically plausible values of γ (Becker et al. 2011; McQuinn & Upton Sanderbeck 2016). We apply flat priors for all the free parameters except for $\tau_{\rm eff}$, where we instead use a Gaussian prior with mean $\tau_{\rm eff} = 1.53$ and a 1σ uncertainty corresponding to 4 per cent of the mean, based on the observational measurement from Becker et al. (2011). The range of $\tau_{\rm eff}$ values on our grid of simulations are $0.7-1.3$ times the mean effective optical depth. If we use a flat rather than Gaussian prior, we find the recovery of the thermal parameters is degraded by the freedom to increase (decrease) the amplitude of the power spectrum on all scales as $\tau_{\rm eff}$ is increased (decreased). In total, we have $9 \times 13 \times 7 \times 7 = 5733$ grid points in our model parameter space. The mock spectra for each parameter combination on this grid of models are post-processed by convolving with a Gaussian instrumental profile of $\mathrm{FWHM} = 7\,\mathrm{km\,s^{-1}}$ and rebinning to $3\,\mathrm{km\,s^{-1}}$ per pixel. Gaussian distributed noise is added and $\tau_{\rm eff}$ is rescaled iteratively to match the required value. Once the model Lyα forest power spectrum parameters are selected, $P_{\rm F}^{\rm model}$ is obtained by performing a multi-linear interpolation on the grid of models.

We match the binning of the Lyα forest power spectrum to mock observations, $P_{\rm F}^{\rm data}$, that we extract from one of our simulations. These consist of 20 data points equally spaced in $\log(k/\mathrm{km^{-1}\,s})$. We consider two simple data scenarios, which we describe as "realistic" and "optimistic". The former is comparable to existing Lyα forest data sets at $z \simeq 5$ (Becker et al. 2015b), while the latter may be more appropriate for observations with high resolution spectrographs on 30 metre class telescopes in the forthcoming decade (e.g. Maiolino et al. 2013). In the realistic case, we consider a total redshift path length of $\Delta z = 4$, a signal-to-noise ratio

[4] We have verified that the gas clumping factor, $C = \langle \rho^2 \rangle / \bar{\rho}^2$, for gas with $\Delta < 10$ in the simulations is also tightly correlated with the gas density power spectrum averaged over the scales used in Fig. 4. The clumping factor is $C \simeq 2$–3 in our models at $z = 4.9$.

[5] For reference, the UVB synthesis models from Faucher-Giguère et al. (2009), Haardt & Madau (2001) and Haardt & Madau (2012) correspond to reionisation at $z_{\rm re}^{\rm FG09} = 10$, $z_{\rm re}^{\rm HM01} = 9$ and $z_{\rm re}^{\rm HM12} = 15$ with $u_0^{\rm FG09} = 7.5\,\mathrm{eV\,m_p^{-1}}$, $u_0^{\rm HM01} = 6.7\,\mathrm{eV\,m_p^{-1}}$ and $u_0^{\rm HM12} = 11.0\,\mathrm{eV\,m_p^{-1}}$ by $z = 4.9$.

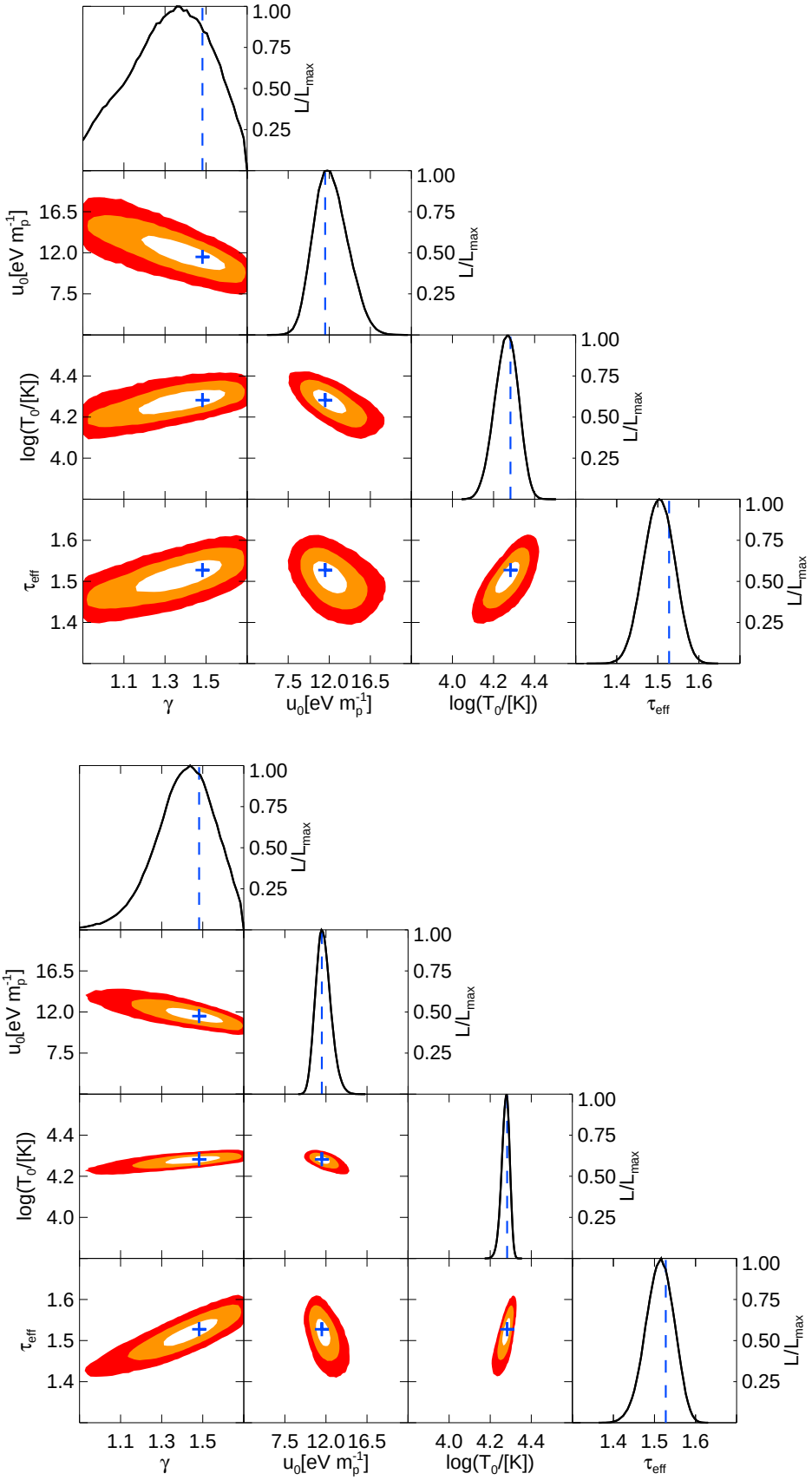

Figure 5. *Top:* The contours display the two dimensional probability distributions for the parameters $\log T_0$, u_0, γ and $\tau_{\rm eff}$ recovered from mock observations of the D15 Lyα forest power spectrum using the realistic data scenario. The joint 1σ, 2σ and 3σ contours are shown in white, orange and red, respectively. The black curves display the one dimensional marginalised posterior distributions for each parameter. The blue cross and blue vertical dashed line show the true model values (see Table 2). *Bottom:* As for the top panel, except now for the optimistic data scenario (see text for further details).

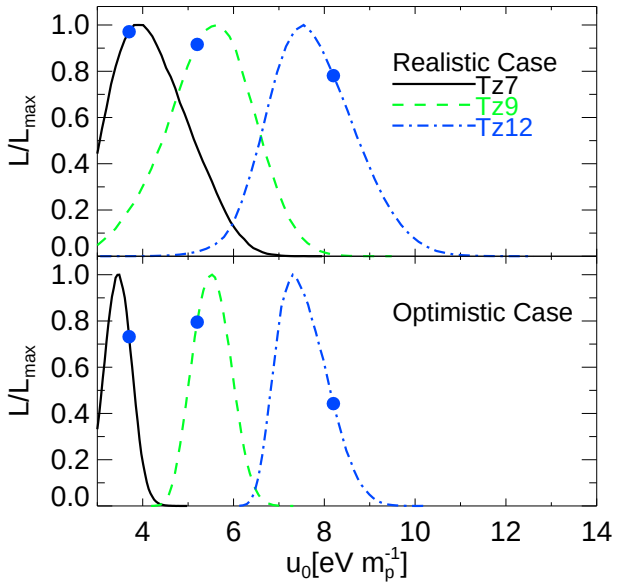

Figure 6. The one dimensional marginalised posterior distributions for u_0 obtained from mock observations of the Tz12 (solid black curve), Tz9 (dashed green curve) and Tz7 (dot-dashed blue curve) simulations. The upper (lower) panels display the realistic (optimistic) data scenario. The true u_0 values at $z < 11.5$ in the simulations are shown by the blue points. These models have very similar values for $\log(T_0)$ and γ at $z \simeq 5$ (see Table 1).

$S/N = 15$ per pixel and bin the power spectrum over the range $-2.3 < \log(k/\mathrm{km^{-1}\,s}) < -0.7$. For the optimistic case, we instead adopt a redshift path length five times larger, $\Delta z = 20$, and a higher signal-to-noise per pixel, $S/N = 50$. The significantly higher signal-to-noise allows the power spectrum to be measured to smaller scales, up to a maximum wavenumber of $\log(k/\mathrm{km^{-1}\,s}) = -0.5$. As demonstrated earlier in Fig. 3, small scale information assists in breaking the degeneracy between thermal broadening and pressure smoothing.

We compute the mean and the distribution for each mock data point by performing 5000 bootstrap samples with replacement. The covariance matrix, $\Sigma_{\rm data}$, is also determined from these distributions. As this matrix can be noisy for real data, following Lidz et al. (2006) and Viel et al. (2013a) we regularise the covariance matrix using the correlation coefficients obtained from all 1000 sight-lines drawn from each simulation. Finally, we increase the 1σ bootstrapped uncertainties by 30 per cent to account for a possible underestimate in the sample variance (Rollinde et al. 2013) and invert the matrix using singular value decomposition. For each mock observation, $P_{\rm F}^{\rm data}$, we perform 10^6 Markov chain iterations and discard the first half of the chain as the burn-in. We verify all chains are converged by visual inspection.

4.2 Distinguishing between reionisation models with $P_{\rm F}(k)$

Table 2 summarises the results of our MCMC analysis for the realistic and optimistic scenarios for a selection of our models (for $\log T_0$ and u_0 only), and Fig. 5 displays the predicted parameter constraints for the D15 model.

In general we find the model parameters are recovered accurately, with only a few exceptions that we shall discuss below. As was (qualitatively) apparent from Fig. 3, we find the power spectrum is rather insensitive to the slope of the T–Δ relation. The parameter γ is recovered within the 68 per cent credible interval but with fairly broad bounds for most of our models, even for the optimistic data set. Fig. 5 indicates it will be difficult to obtain precise constraints on this parameter from the Lyα power spectrum alone at $z \simeq 5$, although probing gas at somewhat higher densities with a joint analysis of the Lyβ forest may improve this situation (Dijkstra et al. 2004; Furlanetto & Oh 2009; Iršič & Viel 2014; Boera et al. 2016). On the other hand, in the absence of significant systematics it should be possible to jointly constrain T_0 and u_0 using existing Lyα forest data at $z \simeq 5$ when including the power spectrum on scales, $\log(k/\mathrm{km^{-1}\,s}) > -1$. Our MCMC analysis indicates that with current data, the cumulative energy deposited per proton at mean density may be constrained to a statistical precision of around ~ 20 per cent, corresponding to the 68 per cent credible interval. The optimistic data scenario instead yields ~ 8 per cent, again at the 68 per cent credible interval. However, as we discuss in the next section, systematic uncertainties from observational and numerical effects will also be important to consider.

The analysis also demonstrates that such a measurement should already be able to distinguish between some reionisation scenarios. The one dimensional posterior distributions for u_0 obtained from the Tz12, Tz9 and Tz7 models are displayed in Fig. 6. Recall that these models have T–Δ relations which are almost identical at $z = 4.9$, but rather different integrated thermal histories. We do not consider the Tz15 model – as already discussed the power spectrum for this model is very similar to the Tz12 simulation. On performing the full MCMC analysis, we recover the cumulative energy input per proton from $4.9 \leq z \leq 11.5$ in the simulations to within 1σ, and at a precision comparable to the results in Fig. 5. Note again, however, that the redshift above which the pressure smoothing scale no longer retains a memory of the thermal history will be model dependent (cf. Pawlik et al. 2009). In addition, we find in this case the peaks of the posterior distributions do not match exactly to the true value of the parameters in the simulations. This is because only the A15–G15 models were used to construct the parameter grid in the MCMC analysis.

As a further demonstration of the model dependent nature of these predicted constraints, we also construct mock observations from the Tz9HOT model where the IGM is heated to around $T \simeq 20000\,\mathrm{K}$ following reionisation. In Fig. 7, it is clear the recovered $\log T_0$ and u_0 are only consistent within the 95 per cent credible interval for the realistic scenario. The smaller statistical error bars obtained in the optimistic case are now inconsistent with the 95 per cent credible interval for u_0. Clearly, an accurate recovery of the thermal history relies on the grid of models used within the MCMC procedure. This suggests that developing a set of numerical models which sample the u_0–$\log T_0$ parameter space as widely and frequently as is practical will therefore be vital for measuring these parameters using observational data.

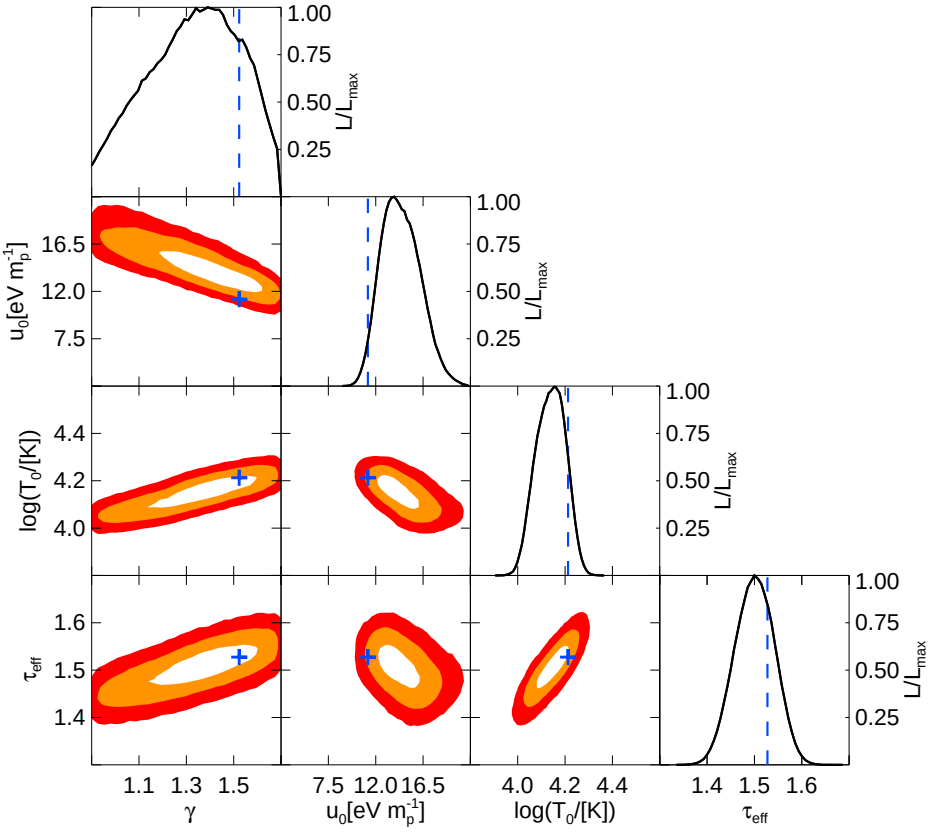

Figure 7. As for Fig. 5, but now for the Tz9HOT model using the realistic data scenario.

Table 2. Predicted constraints on $\log(T_0)$ and u_0 obtained from mock observations for the realistic and optimistic data scenarios (see text for details). From left to right, the columns list the simulation used to construct the mock observation, the parameters used in the simulation and the predicted constraints. The values correspond to the median of the marginalised posterior distribution for each parameter, along with the 68 and 95 per cent credible intervals. The final two rows correspond to the constraints from the mock data after an additional 20 per cent systematic uncertainty in the transmitted flux power spectrum at all scales is added in quadrature to the bootstrap error bars (see text for details).

	Model values		"Realistic" scenario		"Optimistic" scenario	
Model	$\log(T_0/\mathrm{K})$	$u_0[\mathrm{eV\,m_p^{-1}}]$ $4.9 \leq z \leq 11.5$	$\log(T_0/\mathrm{K})$ 68% (95%) C.I.	$u_0[\mathrm{eV\,m_p^{-1}}]$ 68% (95%) C.I.	$\log(T_0/\mathrm{K})$ 68% (95%) C.I.	$u_0[\mathrm{eV\,m_p^{-1}}]$ 68% (95%) C.I.
B15	3.98	5.9	$3.96^{+0.08}_{-0.07}$ $(^{+0.15}_{-0.14})$	$6.1^{+1.0}_{-1.1}$ $(^{+1.9}_{-2.2})$	$3.97^{+0.03}_{-0.03}$ $(^{+0.05}_{-0.05})$	$6.1^{+0.4}_{-0.5}$ $(^{+0.9}_{-1.0})$
D15	4.28	11.5	$4.27^{+0.06}_{-0.06}$ $(^{+0.10}_{-0.12})$	$12.3^{+2.0}_{-1.7}$ $(^{+4.0}_{-3.2})$	$4.28^{+0.02}_{-0.02}$ $(^{+0.03}_{-0.04})$	$11.8^{+0.9}_{-0.8}$ $(^{+1.9}_{-1.4})$
F15	4.47	17.8	$4.47^{+0.04}_{-0.04}$ $(^{+0.07}_{-0.08})$	$18.2^{+1.7}_{-2.2}$ $(^{+2.5}_{-4.0})$	$4.47^{+0.02}_{-0.02}$ $(^{+0.03}_{-0.04})$	$18.0^{+1.3}_{-1.3}$ $(^{+2.4}_{-2.4})$
Tz12	3.93	8.2	$3.95^{+0.06}_{-0.07}$ $(^{+0.11}_{-0.13})$	$7.8^{+1.0}_{-0.9}$ $(^{+2.1}_{-1.7})$	$3.97^{+0.03}_{-0.04}$ $(^{+0.04}_{-0.08})$	$7.5^{+0.6}_{-0.5}$ $(^{+1.2}_{-0.9})$
Tz9	3.92	5.2	$3.90^{+0.09}_{-0.08}$ $(^{+0.16}_{-0.15})$	$5.6^{+0.9}_{-1.0}$ $(^{+1.7}_{-2.0})$	$3.90^{+0.03}_{-0.03}$ $(^{+0.05}_{-0.06})$	$5.6^{+0.4}_{-0.4}$ $(^{+0.8}_{-0.8})$
Tz7	3.93	3.7	$3.89^{+0.07}_{-0.09}$ $(^{+0.12}_{-0.18})$	$4.2^{+0.9}_{-0.7}$ $(^{+1.8}_{-1.1})$	$3.96^{+0.02}_{-0.02}$ $(^{+0.04}_{-0.04})$	$3.5^{+0.3}_{-0.3}$ $(^{+0.6}_{-0.5})$
Tz9HOT	4.21	11.3	$4.15^{+0.06}_{-0.07}$ $(^{+0.11}_{-0.12})$	$14.2^{+2.0}_{-1.7}$ $(^{+4.0}_{-3.0})$	$4.15^{+0.03}_{-0.04}$ $(^{+0.06}_{-0.08})$	$14.1^{+1.0}_{-0.9}$ $(^{+2.1}_{-1.6})$
D15+sys.	4.28	11.5	$4.28^{+0.10}_{-0.09}$ $(^{+0.19}_{-0.17})$	$12.4^{+3.3}_{-3.1}$ $(^{+6.5}_{-6.4})$	$4.27^{+0.05}_{-0.05}$ $(^{+0.11}_{-0.10})$	$12.9^{+3.0}_{-2.5}$ $(^{+6.1}_{-4.7})$
Tz9+sys.	3.92	5.2	$3.90^{+0.13}_{-0.12}$ $(^{+0.22}_{-0.20})$	$5.8^{+1.5}_{-1.5}$ $(^{+3.1}_{-2.5})$	$3.92^{+0.06}_{-0.06}$ $(^{+0.13}_{-0.12})$	$5.5^{+1.3}_{-1.1}$ $(^{+2.7}_{-2.1})$

4.3 Systematic uncertainties

Observational and numerical systematics will also impact on the recovery of u_0 from the transmitted flux power spectrum. These have already been quantified in detail by Viel et al. (2013a) (hereafter V13) in the context of constraining the mass of a putative warm dark matter particle at $z \simeq 5$. However, we also briefly outline these here for completeness and estimate their contribution to the total uncertainty budget.

There are four main sources of systematic uncertainty to consider. Following V13, in approximately ascending order of importance, these are (i) metal line contamination; (ii) the numerical convergence of the simulations; (iii) spatial fluctuations in the ionisation state of the IGM and (iv) continuum placement on the observational data. Note the

impact of galactic outflows on the Lyα forest is expected to minimal by $z \gtrsim 4$ (Viel et al. 2013b).

Narrow metal absorption lines at $z \simeq 5$ arising from CIV, SiIV and MgII at lower redshifts have only a minimal effect (< 1 per cent) on scales $\log(k/\mathrm{km^{-1}\,s}) < -1$ (V13). However, the contribution of metals to the power spectrum may become more important toward smaller scales. We find data at $\log(k/\mathrm{km^{-1}\,s}) > -1$ is important for breaking the degeneracy between thermal broadening and pressure smoothing, and metals may impact here at the ~ 5 per cent level. Corrections to the numerical convergence of the simulations with mass resolution and box size must be applied to the simulations from the results of convergence tests. V13 estimate an additional systematic uncertainty of ~ 5 per cent in addition to this known correction. Spatial fluctuations in the background ionisation rate, particularly if the mean free path for Lyman continuum photons is small and/or the ionising sources are rare (Davies & Furlanetto 2015; Chardin et al. 2015), may have a ~ 10 per cent impact on the power spectrum on the scales of interest here. V13 include this as an additional parameter, $f_{\rm UV}$, which is marginalised over in their MCMC analysis. Finally, the placement of the continuum on high resolution quasar spectra is uncertain at around 10–20 per cent at $z \simeq 5$, which translates to a comparable uncertainty on the amplitude of the power spectrum. In practice, this uncertainty can be forward modelled in the mock spectra (see e.g. V13 and Faucher-Giguère et al. 2008).

We estimate the total systematic uncertainty by adding these contributions in quadrature, yielding ~ 15–25 per cent for the Lyα forest power spectrum on the scales of interest. We estimate the effect on the precision of the measurements by adding in quadrature an additional 20 per cent uncertainty on $P_F(k)$ to our bootstrapped error bars before performing the MCMC analysis. The resulting parameter constraints for the D15 and Tz9 models are displayed in the last two rows of Table 2. This suggests that measurements of u_0 with a total uncertainty of ~ 28 (22) per cent are achievable with the the realistic (optimistic) data scenarios. Improving the precision of this measurement substantially will thus require both higher signal-to-noise data as well as careful forward modelling of the observational and numerical systematics.

5 CONCLUSIONS AND DISCUSSION

In this work we examine the feasibility of constraining the integrated thermal history at $z > 5$ with the Lyα forest using the line of sight transmitted flux power spectrum. We suggest the cumulative energy deposited per proton, u_0, into a gas parcel at mean density at $5 \lesssim z \lesssim 12$ provides a useful parameterisation of the integrated thermal history in our simulations. We demonstrate this quantity correlates well with the underlying gas density power spectrum for $\Delta < 10$ over the scales where pressure smoothing acts in the low density IGM at $z \simeq 5$.

We also note that $z \simeq 5$ observations of the Lyα forest are well suited for this measurement, despite the fact that most of high quality data is available at lower redshifts. This is demonstrated in Fig. 8, which displays the transmitted flux power spectrum for the Tz12 and Tz7 models at $z \simeq 5, 4$ and 3. Recall that both models have very similar instantaneous temperatures at mean density, T_0, at $z < 6$ (see Fig. 1). The differences associated with the thermal history at $z > 6$ are larger at higher redshift; the models are almost indistinguishable by $z = 3$ following the response of the low density gas to changes in the gas pressure and ongoing Hubble expansion. Furthermore, since HeII reionisation is expected to heat the IGM at $z < 5$ (e.g. Becker et al. 2011), higher redshift measurements that potentially avoid this additional heating are desirable for examining HI reionisation.

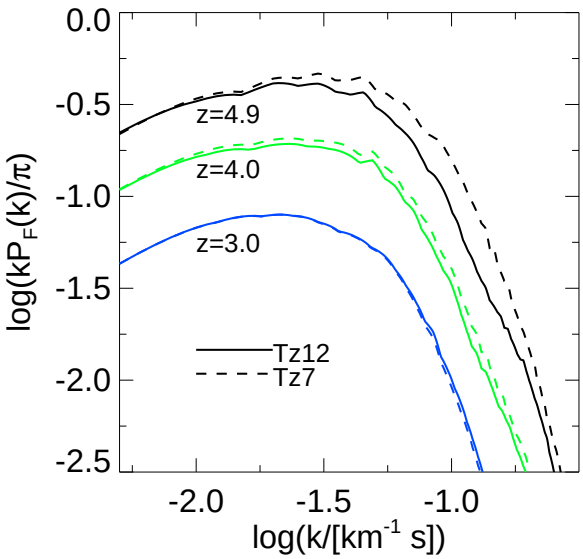

Figure 8. The Lyα forest transmitted flux power spectrum at $z = 4.9$ (black), $z = 4.0$ (green) and $z = 3.0$ (blue) for the Tz12 (solid) and Tz7 (dashed) models. All mock spectra are scaled to have $\tau_{\rm eff} = [1.53, 0.88, 0.39]$ at $z = [4.9, 4.0, 3.0]$ (Becker et al. 2013) and have been convolved with a Gaussian with FWHM=$7\,\mathrm{km\,s^{-1}}$.

We next perform an MCMC analysis of the transmitted flux power spectrum using mock observations drawn from a suite of hydrodynamical simulations. Constraints on the slope of the temperature-density relation, γ, are generally weak at $z \simeq 5$. However, the degeneracy between thermal broadening and pressure smoothing can be broken at $z \simeq 5$ using the power spectrum at scales $\log(k/\mathrm{km^{-1}\,s}) > -1$. We estimate u_0 may be measured with a statistical uncertainty of ~ 20 (~ 8) per cent at $z \simeq 5$ with a redshift path length of $\Delta z = 4$ ($\Delta z = 20$) and a typical signal-to-noise per pixel of S/N = 15 (50) using the power spectrum to scales $\log(k/\mathrm{km^{-1}\,s}) = -0.7$ (-0.5). We note, however, that the constraints are model dependent, and a larger grid of numerical models which explore the full range of the u_0–$\log T_0$ parameter space will be required for an in depth analysis of the observed power spectrum. Estimates for the expected systematic uncertainties (~ 15–25 per cent) are furthermore comparable to the statistical precision attainable with current data. Higher precision measurements are possible only if these systematic uncertainties are minimised in combination with improved signal-to-noise and increased path length.

Including systematic uncertainties, we conclude that currently available data alone should allow for a measurement of u_0 to within ~ 30 per cent at 68 per cent confidence. This corresponds to distinguishing between reionisation scenarios with similar instantaneous temperatures, T_0, at $z \simeq 5$, but an energy deposited per proton that varies by $\simeq 2$–$3\,\mathrm{eV}$

over the redshift interval $5 \leq z \leq 12$. For an initial $T \sim 10^4\,\mathrm{K}$ following reionisation, this corresponds to the difference between early ($z_{\rm re} = 12$) and late ($z_{\rm re} = 7$) reionisation in our models. When compared to predictions of models for the redshift evolution of the ionising background during reionisation – for which u_0 should be straightforward to compute – this will provide an additional and novel constraint on the timing of the reionisation epoch.

ACKNOWLEDGMENTS

The hydrodynamical simulations used in this work were performed with the DiRAC High Performance Computing System (HPCS) and the COSMOS shared memory service at the University of Cambridge. These are operated on behalf of the STFC DiRAC HPC facility. This equipment is funded by BIS National E-infrastructure capital grant ST/J005673/1 and STFC grants ST/H008586/1, ST/K00333X/1. We thank Volker Springel for making GADGET-3 available. FN is supported by a Vice-Chancellor's Scholarship for Research Excellence. JSB acknowledges the support of a Royal Society University Research Fellowship. We thank the anonymous referee for a thoughtful report that helped improve this paper.

REFERENCES

Becker G. D., Bolton J. S., 2013, MNRAS, 436, 1023
Becker G. D., Bolton J. S., Haehnelt M. G., Sargent W. L. W., 2011, MNRAS, 410, 1096
Becker G. D., Hewett P. C., Worseck G., Prochaska J. X., 2013, MNRAS, 430, 2067
Becker G. D., Bolton J. S., Lidz A., 2015a, Publ. Astron. Soc. Australia, 32, 045
Becker G. D., Bolton J. S., Madau P., Pettini M., Ryan-Weber E. V., Venemans B. P., 2015b, MNRAS, 447, 3402
Bi H. G., Boerner G., Chu Y., 1992, A&A, 266, 1
Boera E., Murphy M. T., Becker G. D., Bolton J. S., 2014, MNRAS, 441, 1916
Boera E., Murphy M. T., Becker G. D., Bolton J. S., 2016, MNRAS, 456, L79
Bolton J. S., Becker G. D., 2009, MNRAS, 398, L26
Bolton J. S., Haehnelt M. G., 2007, MNRAS, 374, 493
Bolton J. S., Viel M., Kim T.-S., Haehnelt M. G., Carswell R. F., 2008, MNRAS, 386, 1131
Bolton J. S., Becker G. D., Raskutti S., Wyithe J. S. B., Haehnelt M. G., Sargent W. L. W., 2012, MNRAS, 419, 2880
Bolton J. S., Becker G. D., Haehnelt M. G., Viel M., 2014, MNRAS, 438, 2499
Bouwens R. J., Illingworth G. D., Oesch P. A., Caruana J., Holwerda B., Smit R., Wilkins S., 2015, ApJ, 811, 140
Calura F., Tescari E., D'Odorico V., Viel M., Cristiani S., Kim T.-S., Bolton J. S., 2012, MNRAS, 422, 3019
Cen R., McDonald P., Trac H., Loeb A., 2009, ApJ, 706, L164
Chardin J., Haehnelt M. G., Aubert D., Puchwein E., 2015, MNRAS, 453, 2943
Compostella M., Cantalupo S., Porciani C., 2014, MNRAS, 445, 4186
Croft R. A. C., Weinberg D. H., Bolte M., Burles S., Hernquist L., Katz N., Kirkman D., Tytler D., 2002, ApJ, 581, 20
D' Aloisio A., McQuinn M., Trac H., 2015, ApJ, 813, L38
Davies F. B., Furlanetto S. R., 2015, preprint (arXiv:1509.07131)
Dijkstra M., Lidz A., Hui L., 2004, ApJ, 605, 7
Eisenstein D. J., Hu W., 1999, ApJ, 511, 5
Fan X., et al., 2006, AJ, 132, 117
Faucher-Giguère C.-A., Prochaska J. X., Lidz A., Hernquist L., Zaldarriaga M., 2008, ApJ, 681, 831
Faucher-Giguère C., Lidz A., Zaldarriaga M., Hernquist L., 2009, ApJ, 703, 1416
Finlator K., Oh S. P., Özel F., Davé R., 2012, MNRAS, 427, 2464
Furlanetto S. R., Oh S. P., 2009, ApJ, 701, 94
Furlanetto S. R., McQuinn M., Hernquist L., 2006, MNRAS, 365, 115
Garzilli A., Bolton J. S., Kim T.-S., Leach S., Viel M., 2012, MNRAS, 424, 1723
Garzilli A., Theuns T., Schaye J., 2015, MNRAS, 450, 1465
Gnedin N. Y., 2014, ApJ, 793, 29
Gnedin N. Y., Hui L., 1998, MNRAS, 296, 44
Greig B., Bolton J. S., Wyithe J. S. B., 2015, MNRAS, 447, 2503
Haardt F., Madau P., 2001, in Clusters of Galaxies and the High Redshift Universe Observed in X-rays, Neumann, D. M. & Tran, J. T. V. ed., astro-ph/0106018.
Haardt F., Madau P., 2012, ApJ, 746, 125
Haehnelt M. G., Steinmetz M., 1998, MNRAS, 298, L21
Hui L., Gnedin N. Y., 1997, MNRAS, 292, 27
Hui L., Haiman Z., 2003, ApJ, 596, 9
Hui L., Rutledge R. E., 1999, ApJ, 517, 541
Iršič V., Viel M., 2014, J. Cosmology Astropart. Phys., 12, 024
Katz N., Weinberg D. H., Hernquist L., 1996, ApJS, 105, 19
Kulkarni G., Hennawi J. F., Oñorbe J., Rorai A., Springel V., 2015, ApJ, 812, 30
Lai K., Lidz A., Hernquist L., Zaldarriaga M., 2006, ApJ, 644, 61
Lee K.-G., et al., 2015, ApJ, 799, 196
Lidz A., Malloy M., 2014, ApJ, 788, 175
Lidz A., Heitmann K., Hui L., Habib S., Rauch M., Sargent W. L. W., 2006, ApJ, 638, 27
Lidz A., Faucher-Giguère C.-A., Dall'Aglio A., McQuinn M., Fechner C., Zaldarriaga M., Hernquist L., Dutta S., 2010, ApJ, 718, 199
Lukić Z., Stark C. W., Nugent P., White M., Meiksin A. A., Almgren A., 2015, MNRAS, 446, 3697
Maiolino R., et al., 2013, preprint (arXiv:1310.3163)
McDonald P., Miralda-Escudé J., Rauch M., Sargent W. L. W., Barlow T. A., Cen R., 2001, ApJ, 562, 52
McDonald P., et al., 2006, ApJS, 163, 80
McQuinn M., Upton Sanderbeck P. R., 2016, MNRAS, 456, 47
McQuinn M., Lidz A., Zaldarriaga M., Hernquist L., Hopkins P. F., Dutta S., Faucher-Giguère C.-A., 2009, ApJ, 694, 842
McQuinn M., Hernquist L., Lidz A., Zaldarriaga M., 2011, MNRAS, 415, 977
Meiksin A., 2000, MNRAS, 314, 566
Miralda-Escudé J., Rees M. J., 1994, MNRAS, 266, 343
Mitra S., Choudhury T. R., Ferrara A., 2015, MNRAS, 454, L76
Norman M. L., Reynolds D. R., So G. C., Harkness R. P., Wise J. H., 2015, ApJS, 216, 16
Olive K. A., Skillman E. D., 2004, ApJ, 617, 29
Palanque-Delabrouille N., et al., 2015, J. Cosmology Astropart. Phys., 11, 011
Park H., Shapiro P. R., Choi J.-h., Yoshida N., Hirano S., Ahn K., 2016, preprint (arXiv:1602.06472)
Pawlik A. H., Schaye J., van Scherpenzeel E., 2009, MNRAS, 394, 1812
Pawlik A. H., Schaye J., Vecchia C. D., 2015, MNRAS, 451, 1586
Peeples M. S., Weinberg D. H., Davé R., Fardal M. A., Katz N., 2010, MNRAS, 404, 1281
Planck Collaboration et al., 2015, preprint (arXiv:1502.01589)
Planck Collaboration et al., 2016, preprint (arXiv:1605.03507)
Puchwein E., Bolton J. S., Haehnelt M. G., Madau P., Becker G. D., Haardt F., 2015, MNRAS, 450, 4081
Raskutti S., Bolton J. S., Wyithe J. S. B., Becker G. D., 2012, MNRAS, 421, 1969
Ricotti M., Gnedin N. Y., Shull J. M., 2000, ApJ, 534, 41

Robertson B. E., Ellis R. S., Furlanetto S. R., Dunlop J. S., 2015, ApJ, 802, L19
Rollinde E., Theuns T., Schaye J., Pâris I., Petitjean P., 2013, MNRAS, 428, 540
Rorai A., Hennawi J. F., White M., 2013, ApJ, 775, 81
Rudie G. C., Steidel C. C., Pettini M., 2012, ApJ, 757, L30
Schaye J., 2001, ApJ, 559, 507
Schaye J., Theuns T., Leonard A., Efstathiou G., 1999, MNRAS, 310, 57
Schaye J., Theuns T., Rauch M., Efstathiou G., Sargent W. L. W., 2000, MNRAS, 318, 817
Springel V., 2005, MNRAS, 364, 1105
Springel V., et al., 2005, Nature, 435, 629
Theuns T., Zaroubi S., 2000, MNRAS, 317, 989
Theuns T., Schaye J., Haehnelt M. G., 2000, MNRAS, 315, 600
Theuns T., Schaye J., Zaroubi S., Kim T.-S., Tzanavaris P., Carswell B., 2002, ApJ, 567, L103
Trac H., Cen R., Loeb A., 2008, ApJ, 689, L81
Upton Sanderbeck P. R., D'Aloisio A., McQuinn M. J., 2015, preprint (arXiv:1511.05992)
Verner D. A., Ferland G. J., 1996, ApJS, 103, 467
Viel M., Haehnelt M. G., Springel V., 2004, MNRAS, 354, 684
Viel M., Bolton J. S., Haehnelt M. G., 2009, MNRAS, 399, L39
Viel M., Becker G. D., Bolton J. S., Haehnelt M. G., 2013a, Phys. Rev. D, 88, 043502
Viel M., Schaye J., Booth C. M., 2013b, MNRAS, 429, 1734
Wyithe J. S. B., Loeb A., 2004, Nature, 432, 194
Zaldarriaga M., 2002, ApJ, 564, 153
Zaldarriaga M., Hui L., Tegmark M., 2001, ApJ, 557, 519
Zaroubi S., Viel M., Nusser A., Haehnelt M., Kim T.-S., 2006, MNRAS, 369, 734